Assessment of gas hydrate saturations in the Makran accretionary prism using the offset dependence of seismic amplitudes

Maheswar Ojha[1], Kalachand Sain[1] and Timothy A. Minshull[2]

[1]National Geophysical Research Institute, Uppal Road, Hyderabad - 500 007, India (Council of Scientific and Industrial Research).

E-mail: maheswar_ojha@yahoo.com; kalachandsain@yahoo.com

[2]National Oceanography Centre Southampton, University of Southampton, European Way Southampton SO14 3ZH, UK. E-mail: tmin@noc.soton.ac.uk

ABSTRACT

We estimate the saturations of gas hydrate and free gas based on measurements of seismic reflection amplitude versus offset (AVO) for a bottom simulating reflector (BSR) coupled with rock physics modeling. We apply the approach to data from a seismic line in the Makran accretionary prism in the Arabian Sea. The results reveal lateral variations of gas hydrate and free gas saturations between 4-29% and 1-7.5%, respectively, depending on the rock physics model used to relate seismic velocity to saturation. The approach is simple and easy to implement.

INTRODUCTION

Gas hydrates are crystalline solids of methane and water that are formed at high pressure and low temperature (Kvenvolden, 1998; Sloan, 1998). They have attracted attention because of their widespread occurrence in permafrost and outer continental margins; their potential as future major energy resource; and their role in climate change and geo-hazards (Dillon et al., 1991; Paul et al., 1991; Paull and Dillon, 2001; Milkov et al., 2004; Taylor and Kwan, 2004; Makogon et al., 2007). The identification and quantification of gas hydrate are essential to evaluate their resource potential and assess their associated environmental hazard. Gas hydrate can be identified on multi-channel marine seismic reflection data by mapping an anomalous bottom-simulating reflector (BSR), which marks the base of the high-pressure and relatively low-temperature zone in which hydrates are stable (Andreassen et al., 1990, Kvenvolden et al., 1993). Seismic reflections from BSRs exhibit a wide range of AVO characteristics that depend upon the saturation and distribution of hydrate above and free gas below the BSR (Hyndman and Spence, 1992; Andreassen et al., 1997; Ecker et al., 1998; Carcione and Tinivella, 2000; Yuan et al., 1999). Hydrate may form part of the pore fill or part of the rock matrix, and where present gas may be distributed uniformly or in patches throughout the pore space (Dvorkin et al., 1999; Helgerud et al., 1999). Uniform and patchy gas distributions yield different AVO behaviors because of velocity dispersion in partially gas-saturated sediments (White, 1975; Lee, 2004). We assume a uniform distribution of free gas below the BSR, although the method can be adopted for patchy saturation. Overpressure in the trapped gas also affects the AVO responses, but it is hard to isolate its effect from the effect of gas on P-wave reflection data because both overpressure and free gas can cause low P-wave velocity (Tinivella, 2002). In the hydrocarbon industry, AVO attributes have gained considerable popularity for predicting the lithology and reservoir characteristics (Castagna and Backus, 1993; Castagna and Smith, 1994; Castagna et al., 1998). Several authors

(Hyndman and Spence, 1992; Andreassen et al., 1997; Ecker et al., 1998; Carcione and Tinivella, 2000; Yuan et al., 1999; Chen et al., 2007) have estimated hydrate and/or gas saturations from BSR's using conventional AVO modeling and various rock physics models. Here we present a simple approach that compares the AVO intercept (A) and gradient (B) estimated from the BSR with those from two gas-hydrate models to quantify the saturations of gas-hydrate and free gas across a BSR. For a theoretical calculation of A and B values, we used the Biot-Gassman approach of Lee (2002), and the effective medium theory (EMT) of Helgerud et al. (1999), in both of which hydrate are considered as part of the sediment frame. We demonstrate through a field example in the Makran accretionary prism (Minshull et al., 1992; Sain et al., 2000) that a plot of A versus B can be used to detect free gas below the BSR and quantify the amount of hydrate and gas along a seismic reflection profile.

THEORY

For a plane wave incident at an interface between two semi-infinite isotropic homogeneous elastic half-spaces, and for angles of incidence (θ) up to ~30^0, the P-wave reflection coefficient $R(\theta)$ can be expressed (Shuey, 1985) as

$$R(\theta) \approx A + B\sin^2\theta, \quad \ldots\ldots\ldots\ldots \quad (1)$$

where,

$$A = \frac{1}{2}\left(\frac{\Delta V_P}{V_P} + \frac{\Delta\rho}{\rho}\right) \text{ and } B = AA_0 + \frac{\Delta\sigma}{(1-\sigma)^2}, \quad (2)$$

$$A_0 = B_0 - 2(1+B_0)\frac{1-2\sigma}{1-\sigma},\ B_0 = \frac{\Delta V_P/V_P}{\Delta V_P/V_P + \Delta\rho/\rho},\ V_P = (V_{P2}+V_{P1})/2,\ V_S = (V_{S2}+V_{S1})/2,$$

$$\rho = (\rho_2+\rho_1)/2,\ \Delta V_P = (V_{P2}-V_{P1}),\ \Delta V_S = (V_{S2}-V_{S1}),\ \Delta\rho = (\rho_2-\rho_1),\ \Delta\sigma = (\sigma_2-\sigma_1),$$

$$\sigma = (\sigma_2+\sigma_1)/2 \text{ and } \sigma_i = (0.5V_{Pi}^2 - V_{Si}^2)/(V_{Pi}^2 - V_{Si}^2),\ i = 1, 2.$$

66 V_P, V_S and ρ are the P-wave velocity, S-wave velocity and density respectively. The
67 subscripts 1 and 2 represent the parameters of overlying and underlying layers, respectively.
68 Equations 1-2 are valid for large negative A for a negative impedance contrast across an
69 interface (Castagna et al., 1998; Shuey, 1985), and to about A = 0.2 for a positive impedance
70 contrast (Shuey, 1985).

71 To interpret seismic data in terms of hydrate content, one needs to establish a relation
72 between hydrate saturation in sediments and their velocity. Lee et al. (1996) developed a
73 weighted equation (WE) model, in which hydrate velocities are weighted sum of Wyllie's
74 time average equation (Wyllie et al., 1958) and Wood's equation (Wood, 1941). However,
75 the WE model is not based on physical principles and requires empirical calibration. The
76 velocities predicted from the cementation theory proposed by Dvorkin and Nur (1996) are
77 much higher than those normally observed in nature (Ecker et al., 1998). Helgerud et al.
78 (1999) introduced an EMT that considers the hydrate as part of the rock frame and
79 successfully applied their approach to the P-wave velocity data from Site 995 of ODP Leg
80 164 in the Blake Ridge area. Lee (2002) proposed a method based on Biot–Gassmann theory
81 (BGTL) to relate the elastic properties of sediments to those of the matrix and the pore fluid.
82 Several researchers (Chand et al., 2004; Dai et al., 2004) compared various models and found
83 modest variations in the pattern of velocity with hydrate saturation if the same mineralogy
84 and values of elastic constants are assumed. Here, we use the EMT and BGTL models to
85 calculate the A and B parameters for various gas-hydrate and free gas saturations.

86 In the absence of direct sampling, we assume quartz and clay as mineralogical
87 constituents for the sediment matrix in the Makran (Sain et al., 2000). For a seafloor porosity
88 (ϕ_0) of 60% (Fowler et al., 1985) and a compaction constant λ of 1.17 (Minshull and White,
89 1989), the porosity at the depth of the BSR (~510 m below the seafloor) is calculated as
90 ~39% using the Athy's law ($\phi(z) = \phi_0 e^{(-z/\lambda)}$). Other parameters used in our calculation taken

91 from Lee (2002) are shown in Table 1. The gas density and bulk modulus of methane are
92 calculated to be 0.2 g/cc and 67 MPa respectively at ~ 21° C and 26.34 MPa pressure (Ghosh
93 and Sain, 2008) at BSR depth using Batzle and Wang relation (1992). We use a background
94 P-wave velocity (in absence of gas or hydrate) of 2000 m/s obtained from the normal move
95 out (NMO) interval velocity (described in the next section) for both rock physics models at
96 the BSR depth. This velocity and porosity corresponds to a composition of 10% clay and
97 90% quartz using the EMT model. Assuming the same composition of clay and quartz, the
98 value of consolidation constant 'm' (Lee, 2004) is adjusted to 2.13 in the BGTL model to
99 obtain background velocity of 2000 m/s at the BSR depth. We used the Biot coefficient
100 $\beta = -68.7421/(1+e^{(\phi+0.40635)/0.09425}) + 0.98469$ for unconsolidated marine sediment (Lee,
101 2002, 2004) in the BGTL model. The P- and S-wave velocities decrease with increasing β at
102 a given porosity. A reasonable value of β can be calculated by least-squares fitting of the
103 observed data for a wide range of porosities (Lee, 2002).
104
105 We first compute the A and B attributes using equation 2 by varying the hydrate
106 saturation from 0 to 80% at intervals of 5% for fixed gas saturations of 0, 1, 2, 5 and 10%
107 below the BSR. Above ~10% gas saturation, the P-wave velocity remains almost unchanged.
108 The resulting variations of A as a function of B for 10±5% clay content at 39% porosity and
109 39±2% porosity at 10% clay content are shown in Figure 1 and Figure 2 respectively to
110 demonstrate the effects of clay content and porosity. The porosity is more sensitive than the
111 mineralogical composition to the change in A and B values. In A-B space, a hydrate/brine
112 BSR falls in the 2nd quadrant (negative A and positive B) and is treated as a reference model.
113 The A and B values clearly deviate from this reference trend in presence of gas below the
114 BSR.
115

FIELD DATA

We compute the AVO attributes from seismic data (Figure 3) that show a clear BSR in the Makran accretionary prism (Minshull et al., 1992; Sain et al., 2000). The data have 24 traces in each CDP with a maximum offset of 2559 m and dominant frequency of ~35 Hz. A representative super-gather of CDPs 4378 and 4379 is displayed in Figure 4. The BSR reflection coefficients are calculated from the amplitudes of the seafloor reflection, the BSR and the first multiple of the seafloor reflection using the approach of Warner (1990). The data processing sequence included a band pass filter (4-8-50-60 Hz), a spherical divergence correction ($1/(\text{time} \times \text{velocity}^2)$), minimum phase spiking deconvolution, an NMO correction and trace equalization. The trace to trace or very short wavelength variations are assumed to be noise and need to be eliminated. Trace equalization compensates the amplitude variations due to abnormal shot strength and receiver coupling etc. But it should be applied very cautiously within a long-gate time window (e.g. seafloor to first multiple of seafloor) at the end of all processing steps (Ostrander, 1984; Yu, 1985). Hydrophone directivity is corrected using the function of Sheriff and Geldert (1995). No source directivity correction is applied as the source was of limited spatial extent (Sain et al., 2000). Root-mean-square amplitudes were picked for a time window of 40-50 ms around the BSR, between CDPs 4340 to 4500, where the BSR is strong and relatively flat. The time window was chosen to yield a reliable result despite the change in BSR waveform at CDP 4450. Velocity analysis has been carried out at a 10 CDP interval (225 m). We used a vertically smoothed (20 ms) and spatially averaged NMO interval velocities (Figure 5) to calculate angles of incidence at the BSR using ray theory. Offsets of up to 1610 m have incidence angles of less than 30° and were used in the analysis; results differed little if instead a 25° threshold was used. Reflector depths were obtained by converting the velocity-time function into a velocity-depth function with Dix's formula. A straight line was fit to the averaged interval velocities (Figure 5) which

gives a reference velocity of 2 km/s at the BSR depth. This velocity was used to calibrate the rock physics models. The A and B values and their associated uncertainties (Figure 6a) were derived by weighted least-squares fitting for each supergather of two consecutive CDPs across the section. A running average of A and B over CDP location was superimposed on the theoretical nomogram (Figure 1-2). The running average removes noise from estimated A and B values and potentially reveals lateral changes in hydrate and gas content. Figure 6b illustrates the estimated hydrate and gas saturations with their uncertainties due to uncertainties in A, B and porosity.

DISCUSSION

The A and B attributes are a measure of the normal incidence reflection coefficient (P-wave impedance contrast) and change in Poisson's ratio (a function of both P- and S-wave velocities), respectively. Hence, the A-B crossplot coupled with the rock physics modeling is an important tool for estimation of gas hydrate and free gas respectively. The BGTL model shows almost linear trends with hydrate and gas saturations, whereas the EMT model is more nonlinear (Figure 1-2). At low hydrate saturations (< 10%), the V_P / V_S ratio increases with hydrate saturation because the EMT model predicts little variation in V_S at low hydrate saturation. This complex behavior suggests that it will be difficult to estimate hydrate and gas saturations with the EMT approach when hydrate content is low. The EMT theory predicts higher S-wave velocity than the BGTL theory for any proportion of clay (or quartz) at a specified porosity (for porosity > 30%) and vice versa (Lee 2002; Ojha and Sain, 2008). Thus the predicted background V_P / V_S ratio for the EMT model is always less than that for the BGTL model, and the EMT model always predicts higher hydrate saturation than that of the BGTL model. The BGTL model is more realistic in case of quantification from both V_P and V_S together. The uncertainties in hydrate saturation due to uncertainties in A are small for

166 both the EMT and BGTL models (Figure 6). The maximum uncertainty in hydrate saturation
167 due to uncertainties in B is ±1.5% and ±1.0% using, EMT and BGTL models respectively.
168 The corresponding uncertainties in gas saturation for both models are less than ±0.12%. The
169 largest uncertainties come from the EMT-based estimate due to error in porosity. Uncertainty
170 in estimation of gas saturation may increase with errors in density and bulk modulus of gas
171 which are dependent on pressure and temperature.

172 The presence of gas-rich/gas-poor dipping strata, which produce tuning related highs
173 and lows on amplitudes, and velocity variation at few CDPs in the gas zone below the BSR
174 (Figure 5), complicate the analysis. By using a supergather of two consecutive CDPs and
175 running average of A and B values over a CDP profile, the AB crossplot method gives an
176 overall idea of hydrate and gas in the region. AVO modeling of a synthetic seismogram
177 (Figure 7) shows that the crossplot technique works well where the gas layer is greater than
178 10 m thick. As the thickness of the gas layer decreases, amplitude increases with offset due to
179 tuning between the top and bottom of the gas layer. In an area where the gas layer thickness
180 is unknown, the crossplot technique can be used to extrapolate interpretation away from a
181 small number of selected locations where more time-consuming waveform inversion or
182 modeling techniques are applied, so long as the gas layer is greater than 10 m thick. Tuning
183 effects can lead to localized peaks and troughs in A and B values. By using running means of
184 A and B values over several CDPs, we are able largely to remove these artifacts. The full
185 waveform inversion analysis of two CDP supergathers from the same dataset shows that the
186 gas layer is indeed greater than 10 m thick (Sain et al., 2000). Using high-frequency (up to
187 650 Hz) deep-towed multichannel seismic data, Chapman et al. (2002) delineated a thin, 4-8
188 m negative velocity gradient layer at the BSR on the Vancouver Island margin. However, at
189 lower frequencies, as used here, such thin layers may not be resolved and the BSR commonly
190 appears as a single interface overlying a thick low-velocity zone (e.g., Hyndman and Spence,

1992; Andreassen et al., 1997; Muller et al., 2007; Ecker et al., 1998; Yuan et al., 1999; Carcione and Tinivella, 2000).

Gas hydrates may be distributed in concentrations that are both laterally and vertically variable, controlled by heterogeneities in lithology, permeability and methane transport (Ruppel and Kinoshita, 2000; Trehu et al., 2004; Riedel et al., 2006; Collett et al., 2008; Malinverno et al., 2008). An identifiable reflector is always needed to apply an AVO technique like the A-B crossplot, and in case of gas-hydrate exploration, the reflector is the BSR. The crossplot technique can be used as an effective tool on a regional scale to assess the gas hydrate and free gas saturation at the BSR.

CONCLUSIONS

The A-B crossplot (Figure 1-2) is a nomogram for various rock physics models from which we can (i) understand whether the BSR is underlain by gas and (ii) estimate directly hydrate and gas content. The A and B values derived from the BSR in the Makran accretionary prism deviate clearly from the reference trend and thus indicate the presence of gas below the BSR. The EMT model indicates a hydrate saturation of 14-29% and a gas saturation of 1-6%, while the BGTL model indicates 4-15% hydrate and 1-7.5% gas, respectively, which varies laterally (Figure 6b). The AVO attribute analysis is simple and easy to implement across a wide area to estimate hydrate and gas saturations at a BSR.

ACKNOWLEDGMENTS

We are grateful to the Director, NGRI for his kind consent to publish this work. The Ministry of Earth Sciences and the Department of Science and Technology, New Delhi are acknowledged for their financial support. The associate editor and three anonymous reviewers are thanked for their useful comments and suggestions.

REFERENCES

Andreassen, K., K. Hogstad, and K. A. Berteussen, 1990, Gas hydrate in the southern Barents Sea indicated by a shallow seismic anomaly: First Break, **8**, 235–245.

Andreassen, K., P. E. Hart, and M. Mary, 1997, Amplitude versus offset modeling of the bottom simulating reflection associated with submarine gas hydrates: Marine Geology, **137**, 25-40.

Batzle, W., and Z. Wang, 1992, Seismic properties of pore fluids: Geophysics, **57**, 1396–1408.

Carcione, J. M., and U. Tinivella, 2000, Bottom-simulating reflectors: seismic velocities and AVO effects: Geophysics, **65**, 54-67.

Castagna, J. P., and M. M. Backus, 1993, Offset dependent reflectivity: Theory and Practice of AVO analysis: Society of Exploration Geophysics.

Castagna, J. P., and S. W. Smith, 1994, Comparison of AVO indicators: A modeling study: Geophysics: **59**, 1849-1855.

Castagna, J. P., H. W. Swan, and D. J. Foster, 1998, Framework for AVO gradient and intercept interpretation: Geophysics, **63**, 948-956.

Chand, S., T. A. Minshull, D. Gei, and J. M. Carcione, 2004, Elastic velocity models for gas-hydrate bearing sediments – a comparison: Geophysical Journal International, **159**, 573-590.

Chapman, N. R., J. F. Gettrust, R. Walia, D. Hannay, G. D. Spence, W. T. Wood, and R. D. Hyndman, 2002, High-resolution, deep-towed, multichannel seismic survey of deep-sea gas hydrates off western Canada: Geophysics, **67**, 1038-1047.

Chen, M. P., M. Riedel, R. D. Hyndman, and S. E. Dosso, 2007, AVO inversion of BSRs in marine gas hydrate studies: Geophysics, **72**, C31-C43.

239 Collett, T., M. Riedel, J. Cochran, R. Boswell, J. Presley, P. Kumar, A. Sathe, A. Sethi,
240 M. Lall, V. Sibal, and the NGHP Expedition 01 Scientists, 2008, Indian NGHP
241 Expedition 01 Initial Reports: DGH, India.
242 Dai, J., H. Xu, F. Snyder, and N. Dutta, 2004, Detection and estimation of gas hydrates
243 using rock physics and seismic inversion: Examples from the northern deepwater
244 Gulf of Mexico: The Leading Edge, **23**, 60-66.
245 Dillon, W. P., J. S. Booth, C. K. Paul, K. Fehlhaber, D. R. Hutchinson, and B. A. Swift,
246 1991, Mapping sub-seafloor reservoirs of a greenhouse gas: Methane hydrate:
247 International Symposium on Marine Positioning: Marine Technology Society,
248 Proceedings, 545–554.
249 Dvorkin, J., and A. Nur, 1996, Elasticity of High-Porosity Sandstones: Theory for Two
250 North Sea Datasets: Geophysics, **61**, 1363-1370.
251 Dvorkin, J., D. Moos, J. L. Packwood, and A. Nur, 1999, Identifying patchy saturation
252 from well logs: Geophysics, **64**, 1759-1759.
253 Ecker, C., J. Dvorkin, and A. Nur, 1998, Sediments with gas hydrates: Internal structure
254 from seismic AVO: Geophysics, **63**, 1659–1669.
255 Fowler, S. R., R. S. White, and K. E. Louden, 1985, Sediment dewatering in the Makran
256 accretionary prism: Earth and Planetary Science Letters **75**, 427-438.
257 Fuchs, K., and G. Muller, 1971, Computation of Synthetic Seismograms with the
258 Reflectivity Method and Comparison with Observations: Geophysical Journal
259 Royal Astronomical Society, **23**, 417-33.
260 Ghosh, R., and K. Sain, 2008, Effective medium modeling to assess gas hydrate and free-
261 gas evident from the velocity structure in the Makran accretionary prism, offshore
262 Pakistan: Marine Geophysical Researches, **29**, 267–274.

263 Helgerud, M., J. Dvorkin, A. Nur, A. Sakai, and T. Collett, 1999, Elastic-wave velocity in
264 marine sediments with gas hydrates: Effective medium modeling: Geophysical
265 Research Letters, **26**, 2021–2024.
266 Hyndman, R. D., and G. D. Spence, 1992, A seismic study of methane hydrate marine
267 bottom simulating reflectors: Journal of Geophysical Research, **97**, 6683-6698.
268 Kvenvolden, K. A., 1998, A primer on the geological occurrence of gas hydrate, *in* J. P.
269 Henriet, and J. Mienert, eds., Gas hydrates: Relevance to the World Margin
270 Stability and Climate Change: Geological Society, London, Special Publications,
271 **137**, 9-30.
272 Kvenvolden, K. A., G. D. Ginsburgh, and V. A. Soloviev, 1993, Worldwide distribution
273 of subaquatic gas hydrates: Geo-Marine Letters, **13**, 32–40.
274 Lee, M. W., 2002, Biot-Gassmann theory for velocities of gas-hydrate bearing sediments:
275 Geophysics, **67**, 1711-1719.
276 Lee, M. W., 2004, Elastic velocities of partially gas-saturated unconsolidated sediments:
277 Marine and Petroleum Geology, **21,** 641-650.
278 Lee, M. W., D. R. Hutchinson, T. S. Collett, and W. P. Dillon, 1996, Seismic velocities
279 for hydrate-bearing sediments using weighted equation: Journal of Geophysical
280 Research, **101**, 20347-20358.
281 Makogon, Y. F., S. A. Holditch, and T. Y. Makogon, 2007, Natural gas hydrates — A
282 potential energy source for the 21st Century: Journal of Petroleum Science and
283 Engineering, **56**, 14–31.
284 Malinverno, A., M. Kastner, M. E. Torres, and U. G. Wortmann, 2008, Gas hydrate
285 occurrence from pore water chlorinity and downhole logs in a transect across the
286 northern Cascadia margin (IODP Expedition 311): Journal of Geophysical
287 Research**, 113**, B08103.

Milkov, A. V., 2004, Global estimates of hydrate-bound gas in marine sediments: how much is really out there?: Earth Science Review, **66**, 183-197.

Minshull, T. A., and R. S. White, 1989, Sediment Compaction and Fluid Migration in the Makran Accretionary Prism: Journal of Geophysical Research, **94**, 7387-7402.

Minshull, T. A., R. S. White, P. J. Barton, and J. S. Collier, 1992, Deformation at plate boundaries around the Gulf of Oman: Marine Geology, **104**, 265-277.

Ojha, M., and K. Sain, 2008, Appraisal of gas-hydrates/free-gas from V_P/V_S ratio in the Makran accretionary prism: Marine and Petroleum geology, **25**, 637-644**.**

Ostrander, W. J., 1984, Plane-wave reflection coefficients for gas sands at non-normal angles of incidence: Geophysics, **49**, 1637-1649.

Paull, C. K., and W. P. Dillon, 2001, Natural gas hydrates: occurrence, distribution, and detection: American Geophysical Union, Washington, DC.

Paull, C. K., W. U. III, and W. P. Dillon, 1991, Is the extent of glaciation limited by marine gas-hydrates?: Geophysical Research Letters, **18**, 432–434.

Riedel, M., E. C. Willoughby, M. A. Chen, T. He, I. Novosel, K. Schwalenberg, R. D. Hyndman, G. D. Spence, N. R. Chapman, and R. N. Edwards, 2006, Gas hydrate on the northern Cascadia margin: regional geophysics and structural framework: Proceeding IODP-311, 1-28.

Ruppel, C., and M. Kinoshita, 2000, Fluid, methane, and energy flux in an active margin gas hydrate province, offshore Costa Rica: Earth and Planetary Science Letters, **179**, 153– 165.

Sain, K., T. A. Minshull, S. C. Singh, and R. W. Hobbs, 2000, Evidence for a thick free-gas layer beneath the bottom simulating reflector in the Makran accretionary prism: Marine Geology, **164**, 3-12.

310 Sheriff, R. E., and L. P. Geldert, 1995, Exploration Seismology. History, Theory, Data
311 Acquisition: vol. 1, Cambridge University Press, New York.
312 Shuey, R. T., 1985, A simplification of Zoeppritz equations: Geophysics, **50**, 609-614.
313 Singh, S. C., and T. A. Minshull, 1994, Velocity structure of a gas hydrate reflector at
314 Ocean Drilling Program site 889 from a global seismic waveform inversion:
315 Journal of Geophysical Research, **99**, 24221–24233.
316 Sloan, E. D., 1998, Clathrate Hydrate of Natural Gases: Marcel Dekker, New York.
317 Taylor, C. E., and J. T. Kwan, 2004, Advances in the study of gas-hydrates: Kluwer
318 Academic/Plenum Publishers, New York.
319 Tinivella, U., 2002, The seismic response to overpressure versus gas hydrate and free gas
320 concentration: Journal of Seismic Exploration, **11**, 283-305.
321 Trehu, A. M. et al., 2004, Three-dimensional distribution of gas hydrate beneath southern
322 Hydrate Ridge: constraints from ODP Leg 204: Earth and Planetary Science
323 Letters, **222**, 845–862.
324 Warner, M., 1990, Absolute reflections from deep seismic reflections: Tectonophysics,
325 **173**, 15-23.
326 White, J. E., 1975, Computed seismic speeds and attenuation in rocks with partial gas
327 saturation: Geophysics, **40**, 224-232.
328 Wood, A. B., 1941, A Textbook of Sound: Macmillan, New York, **pp** 578.
329 Wyllie, M. R. J., A. R. Gregory, and G. H. F. Gardner, 1958, An experimental
330 investigation of factors affecting elastic wave velocities in porous media:
331 Geophysics, **23**, 459-493.
332 Yu, G., 1985, Offset-amplitude variation and controlled-amplitude processing:
333 Geophysics, **50**, 2697-2708.

Yuan, T., G. D. Spence, R. D. Hyndman, T. A. Minshull, and S. C. Singh, 1999, Seismic velocity studies of a gas hydrate bottom-simulating reflector on the northern Cascadia continental margin: Amplitude modeling and full waveform inversion: Journal of Geophysical Research, **104**, 1179-1191.

Figure captions

Figure 1. Theoretical crossplots between intercept (A) and gradient (B) computed using varying saturation of gas hydrates with several fixed saturation of free gas based on (a) BGTL and (b) EMT models respectively, prepared for 10±5% clay content and 39% porosity. Running average of A and B values (plus signs) estimated for various CDP locations are superimposed.

Figure 2. Theoretical crossplots between intercept (A) and gradient (B) computed using varying saturation of gas hydrates with several fixed saturation of free gas based on (a) BGTL and (b) EMT models respectively, prepared for 39±2% porosity (ø) and 10% clay content. Running average of A and B values (plus signs) estimated for various CDP locations are superimposed.

Figure 3. Seismic stacked section along a south-north seismic line in the Makran accretionary prism. Inset shows the study area. The BSR shows crosscutting with dipping strata, opposite polarity with respect to the seafloor reflection and mimicking the seafloor topography.

Figure 4. A representative NMO corrected super gather of CDP 4378 and 4379 showing reflections from the seafloor, BSR and the first multiple of seafloor reflection. Amplitudes of the multiple and seafloor are used to calculate reflection coefficients of the BSR.

Figure 5. Thin lines show smooth NMO interval velocity functions at 10 CDP intervals between CDPs 4340 and 4500. Thick solid line shows spatially averaged interval velocity with depth. Dashed line is a straight line fitted to the averaged interval velocity (solid line).

Figure 6. (a) A and B values (with error bars) against the CDPs, estimated based on weighted least square fit and then running average for less than 30º angle (1610 m offset) and (b) hydrate and gas saturations against CDPs, estimated by EMT and BGTL models respectively

362 at 39±2% porosity and 10% clay content. Error bars are due to errors in A (small bars) and B
363 (large bars) at 39% porosity.
364 **Figure 7.** Modeled amplitudes of the BSR normalized with respect to the seafloor for several
365 thicknesses of hydrate and free gas layers (in sets). Velocity-depth functions are computed
366 using BGTL theory for 20% hydrate and 2% gas with Q-factor 250 and 150 (Singh and
367 Minshull, 1994) respectively. The synthetic seismograms are generated using the reflectivity
368 method (Fuchs and Mueller, 1971) with the frequency band of 2-10-80-94 Hz. Thick gas
369 layers result in negligible tuning effects (a and b). However, considerable effects are
370 observed when underlying gas layer is less than 10 m thick (c).
371

Table 1. Parameters used in theoretical calculations (Lee, 2002)

Component	K (GPa)	G (GPa)	ρ (g/cc)
Quartz	36	45	2.65
Clay	20.9	6.85	2.58
Hydrate	6.41	2.54	0.91
Methane*	0.067	-	0.20
Water	2.25	-	1.00
Critical Porosity 36%, No of grain/contact 9, N=1			
* Ghosh and Sain (2008)			

382

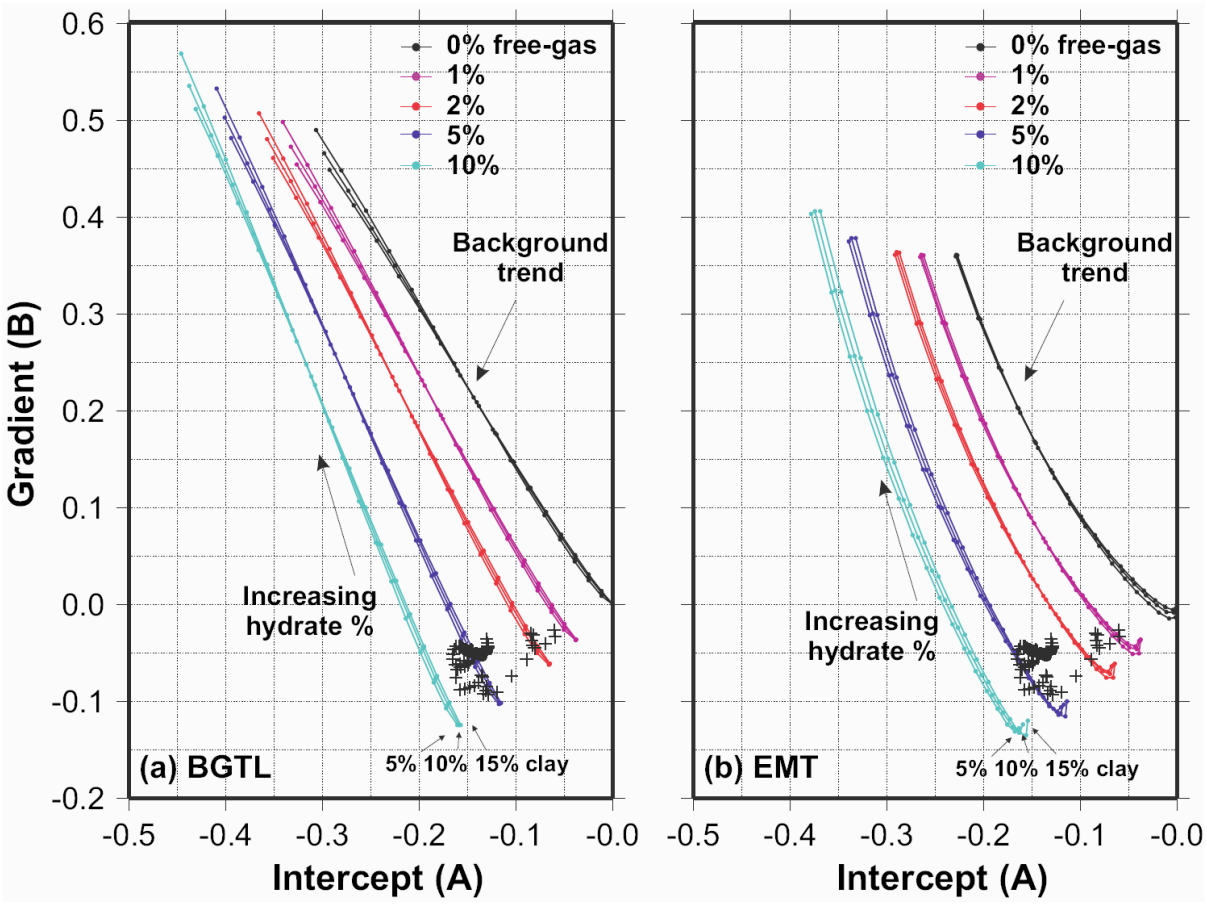

383

384 Figure 1

385

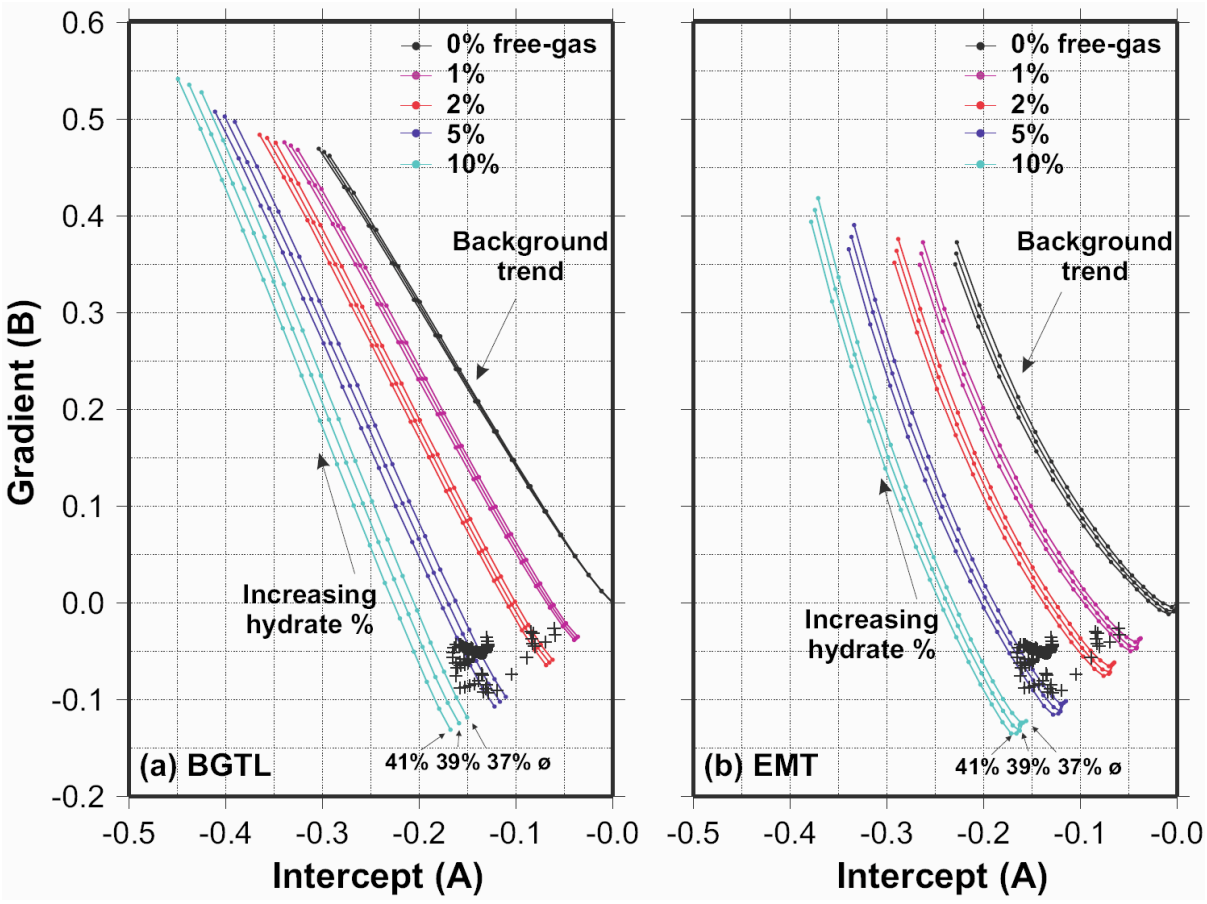
0% free-gas
1%
2%
5%
10%
Background trend
Increasing hydrate %
41% 39% 37% ø
(a) BGTL
(b) EMT
Gradient (B)
Intercept (A)
0.6
0.5
0.4
0.3
0.2
0.1
0.0
-0.1
-0.2
-0.5
-0.4
-0.3
-0.2
-0.1
-0.0

Figure 2

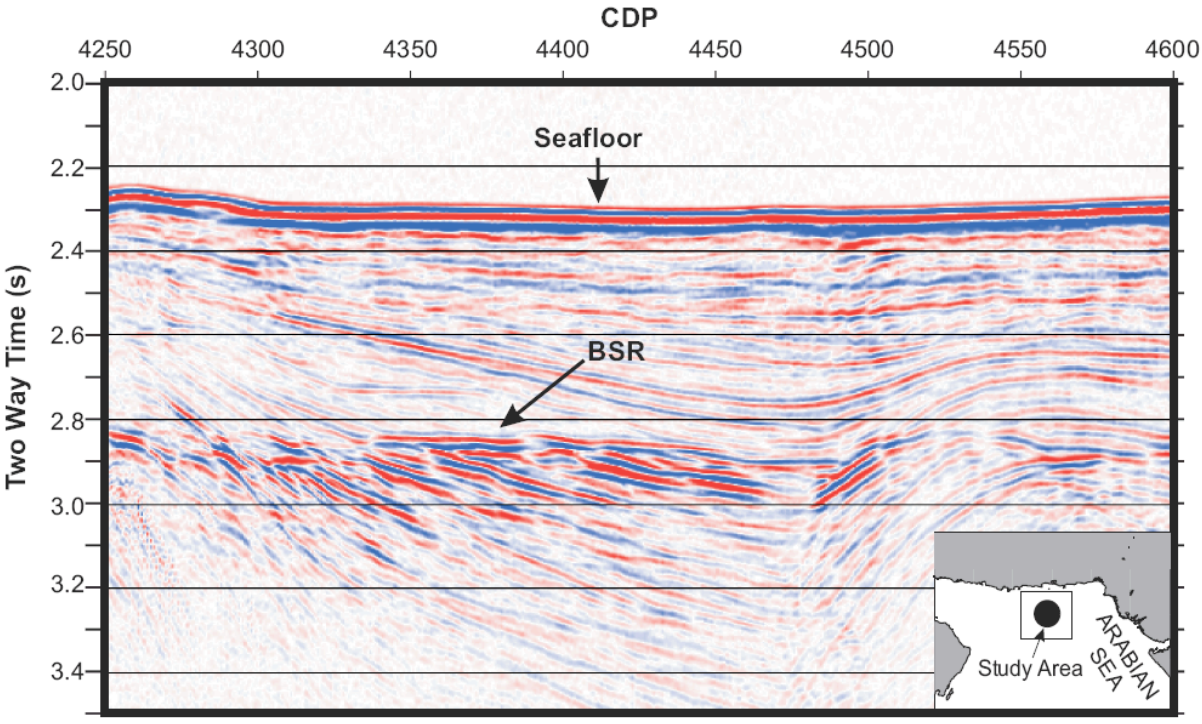
CDP
4250
4300
4350
4400
4450
4500
4550
4600
2.0
2.2
2.4
2.6
2.8
3.0
3.2
3.4
Two Way Time (s)
Seafloor
BSR
Study Area
ARABIAN SEA

Figure 3

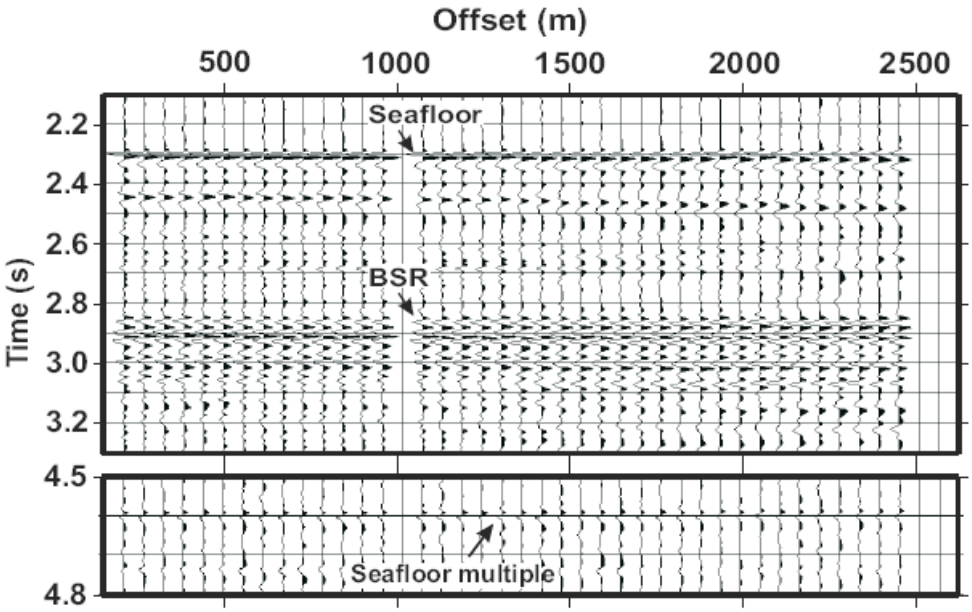
Offset (m)
500
1000
1500
2000
2500
Time (s)
2.2
2.4
2.6
2.8
3.0
3.2
4.5
4.8
Seafloor
BSR
Seafloor multiple

Figure 4

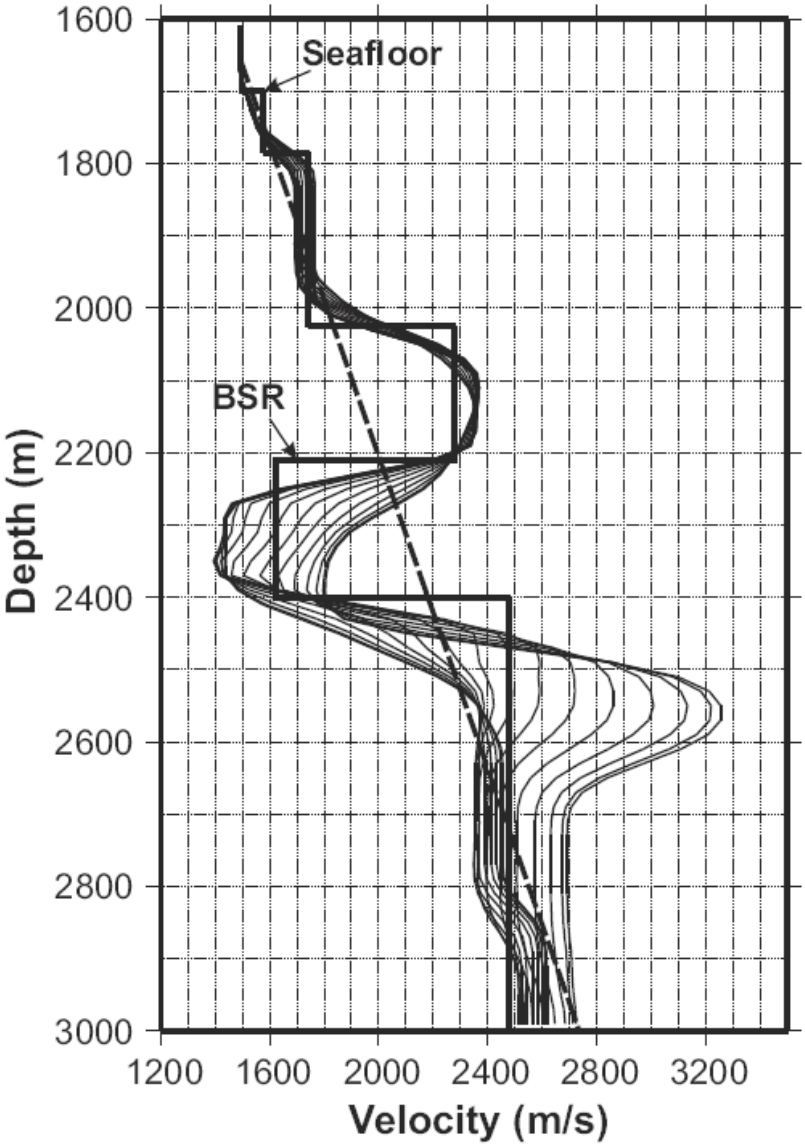
Seafloor
BSR
Depth (m)
1600
1800
2000
2200
2400
2600
2800
3000
1200
1600
2000
2400
2800
3200
Velocity (m/s)

Figure 5

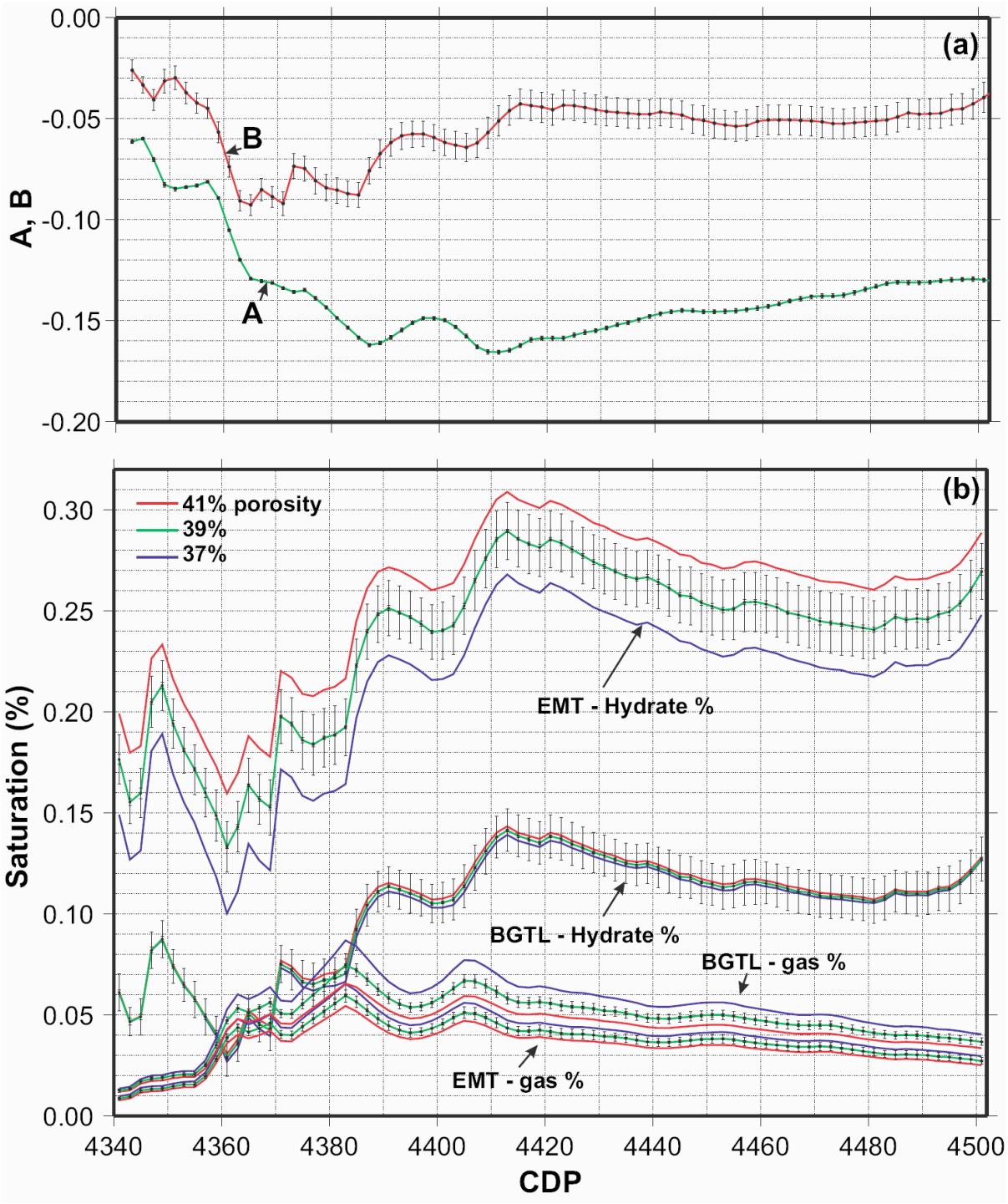
(a)
A, B
B
A
0.00
-0.05
-0.10
-0.15
-0.20
(b)
41% porosity
39%
37%
EMT - Hydrate %
BGTL - Hydrate %
BGTL - gas %
EMT - gas %
Saturation (%)
0.30
0.25
0.20
0.15
0.10
0.05
0.00
4340
4360
4380
4400
4420
4440
4460
4480
4500
CDP

Figure 6

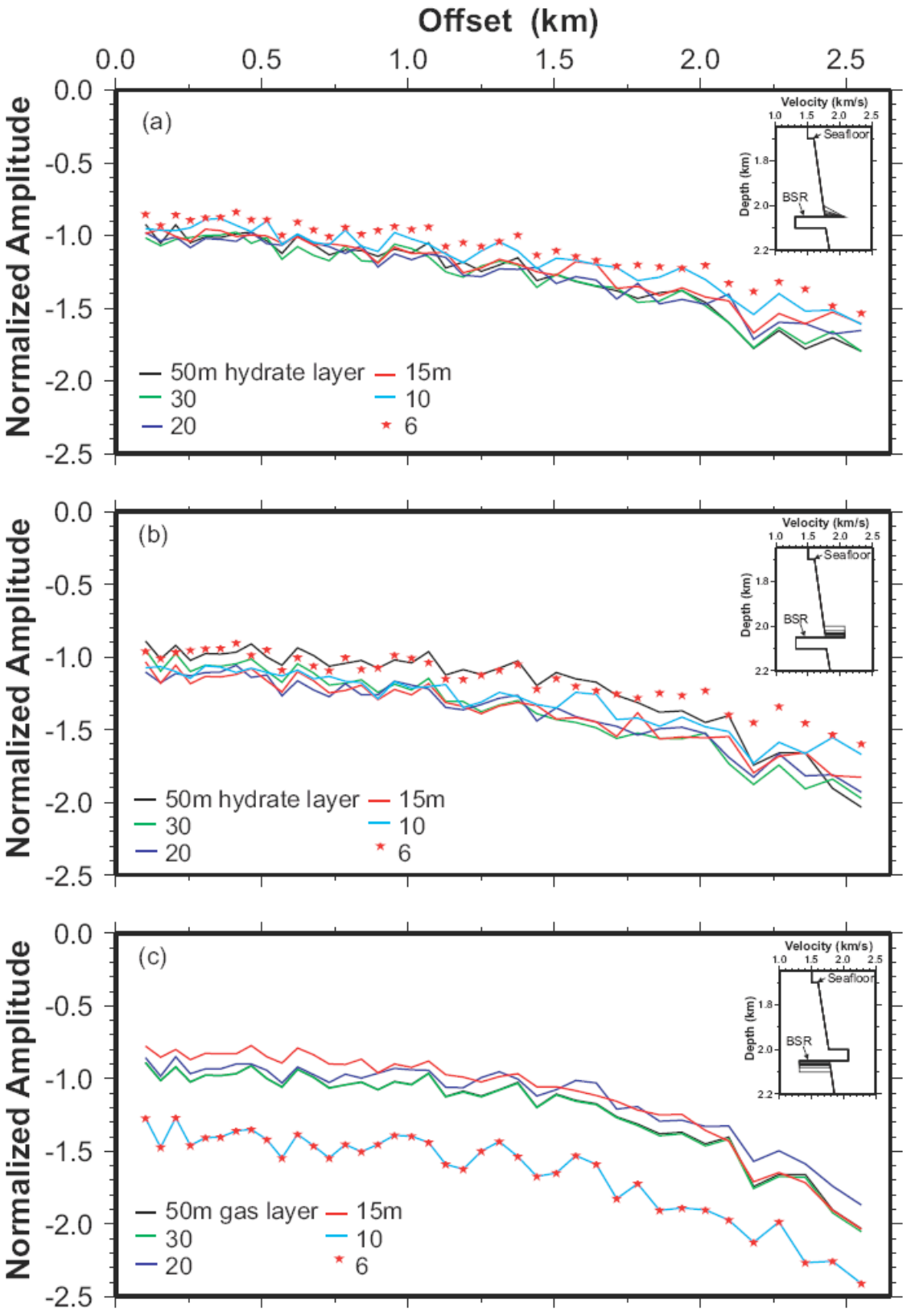

446

447 Figure 7